

# Clinically applicable deep learning-based decision aids for treatment of neovascular AMD

M. Gutfleisch, MD <sup>1,6</sup>, O. Ester <sup>2</sup>, S. Aydin <sup>2</sup>, M. Quassowski <sup>2</sup>, G. Spital, MD <sup>1,6</sup>, A. Lommatzsch, MD <sup>1,3,4,6</sup>, K. Rothaus <sup>1,6</sup>, A. M. Dubis, PhD <sup>5</sup>, D. Pauleikhoff, MD <sup>1,3,4,6</sup>

<sup>1</sup>Department of Ophthalmology, St. Franziskus-Hospital, Muenster, Germany

<sup>2</sup>Westphalia DataLab GmbH, Muenster, Germany

<sup>3</sup>Department of Ophthalmology, University Duisburg-Essen, Essen, Germany

<sup>4</sup>Achim Wessing Institute of Ophthalmic Diagnostic, University Duisburg-Essen, Essen, Germany

<sup>5</sup>NIHR Biomedical Resource Centre at UCL Institute of Ophthalmology and Moorfields Eye Hospital NHS Trust, London, United Kingdom of Great Britain and Northern Ireland

<sup>6</sup>M<sup>3</sup> Macula Monitor Muenster GmbH & Co KG, Muenster, Germany

Key messages

- Decisions for treatment of neovascular AMD are often challenging for non-retina specialists.
- Initial and repeated indication of anti-VEGF therapy in neovascular AMD can be assisted using deep learning network analysis.
- The algorithm can be supervised by activation map volume scan visualization.

## Acknowledgments:

H. Faatz, MD <sup>1,6</sup>, as a retina specialist, he was involved in analysing the saliency maps.

B. Heimes-Bussmann, MD <sup>1,6</sup>, M. Ziegler, MD <sup>1,6</sup>, as retina specialists, they were involved in benchmarking the AI analysis of the initial indication and in analysing the saliency maps.

**Corresponding Author:** Dr. med. Matthias Gutfleisch, Department of Ophthalmology, St. Franziskus-Hospital, Hohenzollernring 74, 48145 Muenster, Germany; phone: +492519352731, fax: +492519352719, email: Matthias.Gutfleisch@augen-franziskus.de

27 **ORCID:** M. Gutfleisch: 0000-0002-2001-5838, O. Ester: 0000-0003-3412-5605, S. Aydin:  
28 0000-0001-9791-7517, M. Quassowski: 0000-0001-6018-2385, G. Spital: -, A. Lommatzsch:  
29 0000-0001-9640-4103, K. Rothaus: 0000-0002-4288-8795, A. M. Dubis: 0000-0002-5108-  
30 2179, D. Pauleikhoff: 0000-0003-3691-291X  
31 Keywords: neovascular age-related macular degeneration (nAMD), anti-VEGF therapy,  
32 artificial intelligence, deep learning network, convolutional neural network, treatment  
33 algorithms

34 **Abbreviations**

35 AI: artificial intelligence

36 AMD: age-related macular degeneration

37 AUC: area under curve

38 BCVA: best corrected visual acuity

39 BM: Bruch's membrane

40 CATT trial: Comparison of Age-related Macular Degeneration Treatment Trials: Lucentis-  
41 Avastin Trial

42 CNN: convolutional neural network

43 CNV: choroidal neovascularization

44 FA: fluorescein angiography

45 ILM: inner limiting membrane

46 IVAN trial: Inhibition of VEGF in Age-related choroidal Neovascularisation trial

47 GPU: graphics processing unit

48 LSTM: long short-term memory

49 M: mean score

50 nAMD: neovascular age-related macular degeneration

51 PRN: pro re nata

52 RC reading centre

53 RPE: retinal pigment epithelium

54 ROC: receiver operating characteristic

55 ReLU: rectified linear unit

56 SD: standard deviation

57 SD-OCT: spectral domain optical coherence tomography

58 tanh: hyperbolic tangent

59 TNR: true negative rate

60 TPR: true positive rate

61 VEGF: vascular endothelial growth factor

62 **Abstract**

63 **Purpose:** Anti-Vascular Endothelial Growth Factor (Anti-VEGF) therapy is currently seen as  
64 the standard for treatment of neovascular AMD (nAMD). However, while treatments are highly  
65 effective, decisions for initial treatment and retreatment are often challenging for non-retina  
66 specialists. The purpose of this study is to develop convolutional neural networks (CNN) that  
67 can differentiate treatment indicated presentations of nAMD for referral to treatment centre  
68 based solely on SD-OCT. This provides the basis for developing an applicable medical decision  
69 support system subsequently.

70 **Methods:** SD-OCT volumes of a consecutive real-life cohort of 1503 nAMD patients were  
71 analysed and two experiments were carried out. To differentiate between no treatment class vs.  
72 initial treatment nAMD class and stabilised nAMD vs. active nAMD two novel CNNs, based  
73 on SD-OCT volume scans, were developed and tested for robustness and performance. In a step  
74 towards explainable artificial intelligence (AI), saliency maps of the SD-OCT volume scans of  
75 24 initial indication decisions with a predicted probability of >97.5% were analysed (score 0-2  
76 in respect to staining intensity). An AI benchmark against retina specialists was performed.

77 **Results:** At the first experiment the area under curve (AUC) of the receiver operating  
78 characteristic (ROC) for the differentiation of patients for the initial analysis was 0.927  
79 (standard deviation (SD): 0.018), for the second experiment (retreatment analysis) 0.865 (SD:  
80 0.027). The results were robust to downsampling ( $\frac{1}{4}$  of the original resolution) and cross-  
81 validation (10-fold). In addition, there was a high correlation between the AI analysis and expert  
82 opinion in a sample of 102 cases for differentiation of patients needing treatment ( $\kappa = 0.824$ ).  
83 On saliency maps the relevant structures for individual initial indication decisions were the  
84 retina/vitreous interface, subretinal space, intraretinal cysts, subretinal pigment epithelium  
85 space and the choroid.

86 **Conclusion:** The developed AI algorithms can define and differentiate presentations of AMD,  
87 which should be referred for treatment or retreatment with anti-VEGF therapy. This may

- 88 support non-retina specialists to interpret SD-OCT on expert opinion level. The individual
- 89 decision of the algorithm can be supervised by saliency maps.

## 90 **Introduction**

91 Anti-VEGF therapy is currently the standard for the treatment of neovascular age related  
92 macular degeneration (nAMD) [1]. In all prospective studies the minimal inclusion criteria was  
93 “occult (type 1) choroidal neovascularization (CNV) with recent disease progression”. But  
94 analyzing the individual clinical nAMD requiring anti-VEGF therapy using fundus  
95 examination, fluorescein angiography (FA) and spectral domain optical coherence tomography  
96 (SD-OCT) in real-life, a misdiagnosis and disagreement between treating doctors and reading  
97 centres in a range between 5-18% could be identified [2, 3]. Therefore, it is a clinical need to  
98 improve the decision process for anti-VEGF treatment and retreatment of nAMD.

99 Recent years have seen a rapid implementation of artificial intelligence (AI) in medical image  
100 analytics and potential treatment predictions [4–9]. They have been established in subcortical  
101 vascular cognitive impairment [10] and glaucoma [11]. Also, in medical retina these AI  
102 approaches have been shown reliable to differentiate between different macular diseases [7, 8,  
103 12–14]. In addition, previous AI studies in nAMD have shown an acceptable prediction for  
104 conversion of nAMD in the same eye [9, 15] and the second eye [16]. Also the differentiation  
105 of OCT images between normal vs. pathological findings (AMD) [17] as well as the  
106 characterization of specific OCT biomarkers [15–18] could be achieved using AI algorithms.  
107 In this study, we aimed to develop an AI-based decision support for non-retina specialists in  
108 daily clinical work (see Figure 1). Two experiments were carried out for this purpose. The first  
109 experiment aims to differentiate between nAMD patients who need anti-VEGF therapy from  
110 those AMD patients who do not. The second experiment works on facilitating retreatment  
111 decisions (stabilised vs. active nAMD decision) during follow up. In both situations, referral to  
112 a treatment centre would be recommended. To demonstrate the robustness, the algorithms were  
113 tested via cross-validation and benchmarked against multiple retina specialists.

114 The applicability of the approach is underlined by the fact that no specific OCT features were  
115 extracted or annotated, that an end-to-end process was established, that the trained models were  
116 based on image data taken from daily routine treatment, and that special requirements for the  
117 images, such as scan density, were left out and thus the developed AI model can be more easily  
118 used for clinical application.



## 119 **Patients and methods**

### 120 **Overview**

121 OCT scans and treatment decisions were collected during daily practice. For a retrospective  
122 cohort of patients without previous selection where at least one eye was treated following a  
123 standardized treatment protocol, this data was used as input data. For experiment 1, the two  
124 classes are fellow eyes without indication for treatment and eyes requiring treatment. For  
125 experiment 2, the two classes consist of the doctor's assessments of stabilised nAMD or active  
126 nAMD during the course of treatment. Only SD-OCT scans with a standardised resolution made  
127 by Heidelberg Engineering devices were used.

128 A single data preprocessing pipeline and for each experiment a convolutional neural network  
129 (CNN) applying deep learning were developed. Preprocessing consisted of normalizing image  
130 eye side orientation, downsampling to a quarter of the original resolution, removing areas  
131 outside a defined region of interest (ROI) and contrast enhancement. To increase the amount of  
132 training data, the dataset was augmented by variations of the original images randomly rotated  
133 and shifted. 3D convolutional blocks were used in the CNNs so that the models are trained by  
134 all dimensions of the OCT volume. Experiment 1 uses one OCT scan and its target value in a  
135 single CNN. In experiment 2, two subsequent OCT scans of one eye and the corresponding  
136 decision for the latter image were used. Both inputs were processed by one CNN and their  
137 separate outputs combined using a LSTM to also capture temporal information.

138 To demonstrate the robustness of the developed algorithms, cross-validation (10-fold) was  
139 used. In addition, we generated saliency maps of the deep learning model to visualize the  
140 relevant characteristics of the individual deep learning analysis and results of the algorithms.  
141 These saliency map characteristics of initial indication decisions were analysed by retina  
142 specialists (H. F., B. H.-B., M. Z.) for corresponding biomarkers.

143 To benchmark the AI analysis, the results were compared to gradings made by retina specialists  
144 (B. H.-B., M. Z., M. G.) for differentiation of initial indication of patient eyes.

## 145 **Data**

146 The Department of Ophthalmology, St. Franziskus-Hospital, Muenster, Germany, has  
147 established a digital platform between local ophthalmologists and its clinical treatment centre  
148 for cooperative anti-VEGF treatment of patients with nAMD. Using this platform all images  
149 and clinically relevant information are exchanged digitally prior to initial treatment and before  
150 every subsequent treatment [19] with intravitreal anti-VEGF therapy. Decisions for treatment  
151 and retreatment were based on reading centre (RC) analysis at the treatment centre (RC: M<sup>3</sup>  
152 Macula Monitor Muenster GmbH & Co KG, Muenster, Germany). The study used the pro re  
153 nata (PRN) Inhibition of VEGF in Age-related choroidal Neovascularisation (IVAN) [20] trial  
154 protocol (three monthly injections). Treatment and retreatment decision were defined following  
155 the internationally published criteria (Comparison of Age-related Macular Degeneration  
156 Treatments Trials: Lucentis-Avastin Trial [21], IVAN trial [20]).

157 Using this cooperative analysis and treatment system, a consecutive unfiltered cohort of 1503  
158 nAMD patients with SD-OCT volume scans and clinical information was analysed. Patients  
159 were seen between 2012-2020. Clinical information (best corrected visual acuity (BCVA), FA,  
160 gender) and SD-OCT volume scans (Spectralis SD-OCT 1 or 2, Heidelberg Engineering,  
161 Heidelberg, Germany, 49 B-scans, 20° x 20°) were collected. SD-OCT images of fellow eyes  
162 were also transferred to the RC and were used as a comparative cohort. These eyes  
163 demonstrated most often early/intermediate AMD, but a substantial number of eyes also had  
164 disciform scars with BCVA >1.3 logMAR or additional other pathologies like epiretinal gliosis  
165 (Table 1). The study was conducted in compliance with the Declaration of Helsinki. Ethics  
166 Committee (University of Muenster) approval was obtained.

167 Artificial intelligence is based on experience encoded in data. To develop the AI decision  
168 support algorithms, we generated two data sets from this cohort that contain the historical  
169 imaging data from SD-OCT volume scans of AMD-affected patients and their corresponding  
170 treatment decisions from retina specialists. We used these data sets to train and test the  
171 algorithms.

172 The historical SD-OCT image data and meta data were extracted from Heidelberg Engineering's  
173 HEYEX 2 software, which uses a proprietary data format. These files contain the raw pixel data  
174 of the SD-OCT scans, in our case with 49 B-Scans containing 512 A-Scans with 496 pixels.  
175 Additionally, the file's meta data contain SD-OCT segmentation lines automatically generated  
176 by the HEYEX 2 software. The historical patient treatment data at every examination date was  
177 extracted from a structured medical record system. The predefined treatment process supported  
178 by the medical record systems ensures treatment process integrity and the use of structured  
179 treatment forms ensures high data quality.

180 We linked the image and treatment data for each patient based on the image acquisition date  
181 and the medical record date.

### 182 **Data set for experiment 1: no treatment vs. initial treatment**

183 To develop an AI decision support algorithm that differentiates between no treatment vs. initial  
184 treatment of suspicious nAMD cases, we selected all SD-OCT volumes of initial RC  
185 examinations with a nAMD indication and a succeeding intravitreal anti-VEGF therapy  
186 resulting into 1712 eyes with nAMD that required anti-VEGF treatment. SD-OCT images of  
187 fellow eyes without an indication for anti-VEGF-therapy were used as a comparative cohort to  
188 form the no treatment class. The no treatment class contained 737 eyes. All samples of this  
189 class were evaluated by retina specialists to divide it into six subclasses for different stages of  
190 AMD and other pathologies (early AMD, intermediate AMD, geographic atrophy, disciform  
191 scars, nAMD with BCVA >1.3 logMAR, other pathologies).

192 We ensured that only the very first indication of one patient’s eye was included in our data set  
193 since there were patients with multiple AMD indications with treatment gaps of several years.  
194 Overall, this unfiltered data contained 2449 eyes from 1503 patients.  
195 Finally, after filtering for sufficient segmentation lines, 2322 eyes of 1477 patients (1644 eyes  
196 with nAMD that required anti-VEGF treatment and 678 eyes where no treatment was indicated)  
197 were considered in the following experiment. This data underwent the preprocessing steps and  
198 was used for training.

### 199 **Data set for experiment 2: stabilised nAMD vs. active nAMD**

200 The treatment following the IVAN trial protocol makes ongoing AMD examinations of  
201 activation criteria inevitable. Ophthalmologists decide about retreatment with a new anti-VEGF  
202 injection series. To develop a decision support algorithm that helps differentiating between  
203 stabilised vs. active nAMD we assembled a data set that contains historical SD-OCT volumes  
204 and the corresponding retreatment decision. When following the PRN treatment schema, the  
205 decision can either be retreatment (active nAMD class) resulting into a new anti-VEGF  
206 injection series or follow-up visit resulting in a new examination four weeks later (stabilised  
207 nAMD class). We selected every two consecutive SD-OCT volume scans of one initially treated  
208 unique patient eye’s treatment history and the corresponding retreatment decision.

209 For example, from the following ordered images for one patient eye  $SD-OCT_{t-3}$ ,  $SD-OCT_{t-2}$ ,  
210  $SD-OCT_{t-1}$ ,  $SD-OCT_{t_0}$  three unique timeseries-samples were generated:

211 Timeseries sample 1:  $SD-OCT_{t-3}$ ,  $SD-OCT_{t-2}$ , retreatment decision  $t_2$

212 Timeseries sample 2:  $SD-OCT_{t-2}$ ,  $SD-OCT_{t-1}$ , retreatment decision  $t_1$

213 Timeseries sample 3:  $SD-OCT_{t-1}$ ,  $SD-OCT_{t_0}$ , retreatment decision  $t_0$

214 By providing two consecutive SD-OCTs to the CNN, the network can learn to compare both  
215 volumes to make a decision.

216 We also run experiments with only one SD-OCT volume but found out that the AI performance  
217 increases by learning from two consecutive SD-OCTs as seen in the Results section. This

218 coincides with how retina specialists evaluate the development of activation criteria by  
219 examining the preceding and current SD-OCT scans.

220 In total 9451 timeseries samples containing two consecutive SD-OCT volumes were built: 5717  
221 SD-OCT volume scan pairs with decision of stabilised CNV were compared with 3734 SD-  
222 OCT volume scan pairs with decisions for retreatment. Only patient eyes and their follow-up  
223 appointments which previously had been given an initial diagnosis of nAMD needing treatment  
224 (see data set 1) appeared in this dataset.

## 225 **Data Preprocessing**

226 To aid model training, we evaluated several, appropriate image preprocessing methods and  
227 chose the most effective for both experiments. The contribution of each preprocessing step to  
228 the model performance for experiment 1 can be found in the result section and in Table 2. Figure  
229 2 shows the steps of the final data preprocessing pipeline with one sample slice. Raw data of  
230 pixel-wise reflectivity of the SD-OCT scans were separated and manually transferred into the  
231 data preprocessing pipeline. For the analysis, SD-OCT scans with 49 B-Scans containing 512  
232 A-Scans with 496 pixels were filtered from the obtained dataset (volumes with the dimensions  
233 512x496x49). Before feeding the images to the deep learning model, the provided images  
234 underwent preprocessing. No SD-OCT scans were excluded due to image quality, only a small  
235 fraction (up to 7 percent) with non-existent or highly discontinuous segmentation lines was  
236 disregarded, as they were used for the next preprocessing step.

237 A region of interest (ROI) that is considered prognostic of AMD like in Russakoff et al. [9] was  
238 defined so that the CNN focuses on relevant areas only and variance in the dataset is reduced.  
239 For this, the area between the ILM segmentation line and the lower bound of the choroid area  
240 (outer choroidal boundary, OCB) is automatically identified. The areas outside of this ROI (the  
241 vitreous body above the inner limiting membrane (ILM) and the sclera below the choroid) were  
242 replaced with 97% black and 3% low intensity (grey values of 1–64) random noise pixels to

243 improve saliency map interpretability. The ILM segmentation line is produced by the SD-OCT  
244 proprietary software. We used the provided retinal pigment epithelium (RPE) segmentation line  
245 and generated the convex hull around RPE as an estimation of the Bruch's Membrane (BM)  
246 [22]. Following to Russakoff et al. [9] we shifted this BM line down in parallel by 390  $\mu\text{m}$   
247 (empirical mean + 2 SD of the subfoveal choroidal thickness in a population with AMD) to  
248 define a lower bound of the ROI.

249 In the next step, contrast enhancement was applied to the images by using contrast-limited  
250 adaptive histogram equalization (CLAHE).

251 Finally, the dimensions of the B-scans were downsampled to 128x124 by using OpenCV's  
252 interpolation method INTER\_AREA [23], resulting into a volume of 128x124x49. As the  
253 scaling factor 4 is a common divisor of the original dimensions, each resized pixel intensity  
254 shows the average of 4x4 pixels in the original image. Image downsampling is a common  
255 feature in deep learning for ophthalmic image analysis [9, 24]. Downsampling has been done  
256 in both aspect ratio conserving [24] and non-conserving for both OCT [9] and for fundus image  
257 analysis [24]. Lower resolution images as model input allow for faster model training and  
258 parameter tuning in development and use less hardware resources both in training as well as  
259 inference. In addition, it increases transferability of the model to inputs by other SD-OCT  
260 machines with varying resolutions, vendor-specific differences in texture granularity and visual  
261 artefacts. To verify this downsampling does not significantly affect model performance, we  
262 conducted a ceteris paribus comparison for experiment 1 with an adapted CNN design to  
263 account for the bigger input dimensions.

264 To have a more uniform dataset, all images were normalized regarding their horizontal  
265 orientation relative to the nose, meaning images from left eyes were flipped to have the same  
266 orientation as right eyes. To generally enlarge the training data, compensate for natural  
267 variations in scan positioning and alleviate overfitting, the training data was augmented by

268 random rotation (5-10°), vertical shift (3-15%), and horizontal shift (3-10%). We rescaled all  
269 pixel values of 0–255 to floats of 0.0–1.0 to improve the model training convergence speed.  
270 All models were trained end-to-end, without any prior segmentation or biomarker definition.

## 271 **Deep Learning**

272 Both algorithms were trained using end-to-end deep learning, without any prior segmentation  
273 or biomarker definition. Two new deep learning architectures were developed.

### 274 **Architecture experiment 1: no treatment vs. initial treatment**

275 The 3D CNN scheme for experiment 1 consists of three stacked convolutional blocks followed  
276 by a global average pooling and a fully connected dense layers with rectified linear unit (ReLU)  
277 as the activation function. Finally, a softmax layer yields class probabilities for the input  
278 volume. Each convolutional block is composed (of a sequence) of a 3D convolutional layer,  
279 ReLU activation, batch-normalization and a 3D max pooling layer. Table 3 summarizes the  
280 structure and hyper-parameters of the network.

281 To mitigate overfitting, we applied L2-regularization ( $\lambda = 0.005$ ) in the convolutional  
282 layers and dropout in the fully connected layer with a dropout rate of 0.5. Furthermore, early  
283 stopping policy terminated the training once the monitored validation loss had not improved  
284 for multiple epochs. For the final model the weights of the epoch with best performance (lowest  
285 validation loss) were selected.

### 286 **Architecture experiment 2: stabilised nAMD vs. active nAMD**

287 In experiment 2 each sample is treated as a timeseries of two SD-OCT scans, containing the  
288 current and the previous scan from a single patient and eye. Since the input contains spatial and  
289 temporal information, a hybrid model involving a CNN and long-short term memory (LSTM)  
290 was implemented. LSTM is a proven class of model in deep learning used to process sequence  
291 of data. In the proposed model CNN is applied to extract the feature vector representation from  
292 each of the SD-OCT scans, passing the resulting feature vectors to the LSTM for the sequence

293 learning of the above mentioned timeseries. This model architecture was comprised by the 3D  
294 CNN architecture from experiment 1 (here with  $\lambda = 0.0001$ ) as a time-distributed input  
295 to an LSTM layer with 64 hidden cells outputting only the last hidden cell with activated  
296 internal dropout-rate and a recurrent-dropout-rate both of with 0.1, and hyperbolic tangent  
297 ( $\tanh$ ) as the activation function. The output of the LSTM layer is connected to a fully connected  
298 layer with 64 units, and a dropout layer with a dropout-rate of 0.3 concluding to a final softmax  
299 layer for the two-class prediction problem.

### 300 **Training**

301 For training, the whole dataset was first randomly shuffled. To get a reliable evaluation of the  
302 model performance, we conducted 10-fold cross validation at patient level. In each of the 10  
303 training iterations a new rotating subset with 10% of all samples was held out for the test set.  
304 This ensured that each sample was classified once as part of a test set. The remaining samples  
305 were randomly divided into training (72% of all samples) and validation set (18%). To address  
306 data leakage in each iteration all data relating to a patient appeared strictly in one subset only.  
307 The validation sets served for early stopping and best model selection in each iteration. For  
308 overall AUC of an experiment, the mean value of the AUCs from all 10 tests sets was  
309 calculated.

310 Both models were trained by Nadam optimizer [25], with an initial learning rate of 0.001 using  
311 cross entropy as the loss function. In experiment 1 the initial learning rate of 0.001 was adapted  
312 during training to 0.0001 after the 10<sup>th</sup> epochs and then to 0.00001 after 20<sup>th</sup> epoch. Similarly,  
313 in experiment 2, after 20<sup>th</sup> epoch we set the learning rate to 0.005 and to 0.0025 after 30<sup>th</sup> epoch.  
314 The batch size was set to 4. We assessed the prediction performance based on the area under  
315 receiver operating characteristic curve (AUC) score. An AUC of 1 indicates a perfect classifier,  
316 while 0.5 represents a classifier without discriminative power. The receiver operating  
317 characteristic curve (ROC) itself plots the relation between the true positive and false positive



318 rate. In this study we preferred using 3D CNN over 2D CNN topologies, to also capture the  
319 spatial context in the B-scans dimension.

320 A special platform was created for configuring and validating the model parameters, tracking  
321 the experiments, visualizing the results and evaluating the performance. Keras [26] served as  
322 the deep learning framework using TensorFlow [27] as the backend. The experiments ran on a  
323 dedicated machine running Ubuntu Server 20.04 and equipped with two linked GPUs (Nvidia  
324 GeForce Titan RTX, NVIDIA Corporation, Santa Clara, USA).

### 325 **Saliency map viewer**

326 In addition, a saliency map viewer was developed to visualize the relevant characteristics of the  
327 individual deep learning analysis and results of the algorithms using colour coding. Saliency  
328 maps are obtained by computing the partial derivatives of the output class score with respect to  
329 each input image pixel. The magnitude of these partial derivatives denotes the contribution of  
330 each pixel to the predicted class [28, 29]. For improved interpretation a gaussian filter with a  
331 standard deviation value of 0.8 is applied to smooth out the resulting/calculated pixel values of  
332 the saliency map. Highly activated areas are highlighted in red to yellow colour.

### 333 **Grading by retinal specialists**

334 To compare our results with human decision making, we let three retina specialists perform a  
335 grading of 102 randomly chosen samples. Each grader was given the original full resolution  
336 SD-OCT volume scan used in the initial indication without any additional clinical information  
337 to differentiate between treatment and no treatment.

## 338 **Results**

### 339 **Experiment 1: no treatment vs. initial treatment**

340 In experiment 1, besides the final scores, we also determined the effects of the different  
341 preprocessing steps to evaluate their usefulness for the model. Without any preprocessing  
342 except resizing each B-scan to 1/4th of the original resolution a model was trained with an AUC  
343 of 0.880 to serve as a baseline for iteratively evaluating the usefulness of further preprocessing  
344 steps. All values were recorded with 10-fold cross validation. By utilizing the ROI enhancement  
345 preprocessing step after resizing the AUC increased to 0.906. Additionally, applying CLAHE,  
346 the mean AUC improved to 0.925. To verify that our downsampling did not significantly affect  
347 model performance, we conducted a ceteris paribus comparison for the preprocessing pipeline  
348 with ROI enhancement and CLAHE applied but using full-sized images with an adapted CNN  
349 design to account for the bigger input dimensions. This showed that using full-sized images and  
350 the resulting bigger variance in samples produced lower AUC of 0.903 (SD: 0.018), indicating  
351 that our sample size did not suffice for the increased number of features in the full-size image.  
352 By extending the preprocessing pipeline of ROI enhancement, CLAHE and downsampling with  
353 augmentation, the final AUC showed a slight improvement: The model for initial indication  
354 achieved a mean AUC of 0.927 (standard deviation (SD): 0.018). Figure 3 depicts the single  
355 ROCs, the mean ROC and the standard deviation of all ten runs. Additionally, an operating  
356 point for the optimal operating threshold according to Zweig and Campbell [30] with equal  
357 costs for all decisions ( $m = 1$ , so TPR-TNR is maximized) is given. Also, the frequency of the  
358 prediction value was analysed to evaluate the effectiveness of the network (Figure 4). Among  
359 all instances the model predicts with high confidence the correct class with only small portion  
360 of misclassifications. Especially for true predictions of initial treatment a high frequency of  
361 confidence values close to 1.0 was observed, while most true predictions of no treatment had a

362 confidence value of at least 0.8. This validates the model's capacity discriminating no treatment  
363 versus initial treatment decisions with high confidences.

364 To further understand the model performance, all samples of the no treatment class were  
365 grouped by their respective subclass as described in the Data section. The number of correct  
366 “no treatment” (true negative) and incorrect “initial treatment” (false positive) predictions for  
367 the default decision threshold of 0.5 as well as the true negative rate (TNR or specificity) per  
368 subclass can be seen in Table 1. For samples with no treatment AMD the model showed the  
369 highest subclass TNR of 91% across both classes. Especially eyes with BCVA >1.3 logMAR,  
370 where treatment is generally not considered, leads to a low subclass TNR of 55%. Even with  
371 this irregular real-life dataset, a big majority of patients requiring no treatment were correctly  
372 predicted as such, with a true negative rate (TNR) of 80%. When pruning the no treatment class  
373 by removing all subclasses except early/intermediate AMD, model performance could be  
374 improved significantly to a TNR of 97%. The mean AUC increased from 0.927 with real-life  
375 data to 0.976 with pruned data. This indicates that improvements for real-life applications could  
376 be reached by automatic filtering of known properties (like BCVA) or using a multiclass model  
377 which differentiates between characteristic subclasses.

## 378 **Experiment 2: stabilised nAMD vs. active nAMD**

379 Using the dataset without augmentation but with the final preprocessing pipeline the model for  
380 differentiation of stabilised vs. active nAMD achieved a mean AUC of 0.842 (SD: 0.022). By  
381 applying augmentation, the performance increased to a mean AUC of 0.865 (SD: 0.027; Figure  
382 5), which is the final AUC for experiment 2.

383 We were also interested to assess the benefit of utilizing preceding and current SD-OCT as a  
384 timeseries against the case of only using the current SD-OCT as input. For the case of using a  
385 single SD-OCT volume as input, the deep learning model consisted of the 3D-CNN part of our  
386 3D-CNN-LSTM architecture only. For this comparison, datasets without augmentation were  
387 used. The model with the single (current) SD-OCT volume achieved an AUC of only 0.815

388 (SD: 0.027), compared to the AUC of 0.842 (SD: 0.022) in the timeseries case using the LSTM  
389 architecture.

390 Also, the frequency of the prediction value was analysed to evaluate the effectiveness of the  
391 network (Figure 6). For true predictions of stabilised nAMD a high frequency of confidence  
392 values close to 1.0 was observed, while most true predictions of active nAMD had a confidence  
393 value of at least 0.8. This validates the model's capacity discriminating stabilised nAMD versus  
394 active nAMD decisions with high confidences.

### 395 **Saliency map analysis**

396 Figure 7a shows the saliency map for a single B-scan direction with highly activated areas in  
397 red to yellow colour. Figure 7b is showing the saliency map in direction across all 49 B-scans.  
398 Since the areas, which demonstrated activation, are continuous between adjacent B-scans, it is  
399 indicating the value of using 3D CNN instead of 2D CNN. In the 3D CNN different structures  
400 (interface vitreous/retina, subretinal, intraretinal, sub-RPE space and choroid) could be  
401 differentiated. To define a gradation of the relevant structures, on which the algorithm decided  
402 towards an individual recommendation (red coded structure), the saliency maps of 24 patients  
403 with a predicted probability of  $\geq 97.5\%$  and an active stage of the nAMD were analysed. Scores  
404 from 0-2 (0 = no staining, 1 = slight staining, 2 = intensive staining) were used for each  
405 morphological structure and a mean score (M) was registered. This analysis of colour intensity  
406 on individual saliency maps was applied on complete volume scans by two independent graders  
407 using standard images for classification. The retina/vitreous interface was the most important  
408 structure relevant for the activity decision of the algorithm (M = 2.0; SD  $\pm$  0). This is followed  
409 by the subretinal space (M = 1.375; SD  $\pm$  0.770), the intraretinal cysts (M = 1.0; SD  $\pm$  0.933),  
410 the sub-RPE space (M = 0.667; SD = 0.868) and the choroid (M = 0.625; SD  $\pm$  0.824).  
411 Therefore, using the saliency map analysis, the deep learning model could visualize areas in the  
412 SD-OCT images, which are relevant for an individual decision and therefore the results of the  
413 AI algorithm can be correlated with typical corresponding retinal AMD changes.

#### 414 **Comparison with retinal specialists**

415 The metrics of manual grading can be seen in Table 4. The results for grading with only SD-  
416 OCT volume information available show a high interrater reliability with a Fleiss' Kappa [31]  
417 of  $\kappa = 0.824$ . As ground truth, the decisions by doctors in our real-life dataset were used and  
418 compared to the majority vote of the three retinal specialists. A Cohen's Kappa value of  $\kappa =$   
419  $0.776$  was observed. Sensitivity for each grader ranged from 78 to 94% (majority vote: 91%),  
420 specificity from 78 to 91 % (majority vote: 87 %). All false evaluations by majority vote were  
421 looked at manually: the 6 false negatives can be explained by unicus situation and activity  
422 which is only visible in other imaging modalities than SD-OCT images, while the remaining 4  
423 false positives either had BCVA  $>1.3$  logMAR or disciform scars.

424 The grading performance can be compared to our predictions made in 10-fold cross-validation  
425 for these 102 samples as they are based on the same image data. Again, the doctors' clinical  
426 decisions were used for comparison. With the default decision threshold of 0.5 a Cohen's Kappa  
427 of  $\kappa = 0.650$  was observed for all model predictions, being close to human performance.

## 428 **Discussion**

429 In this study using an unspecified real-life cohort of nAMD patients two new CNNs have been  
430 developed, which can support non-retina specialists to distinguish between AMD cases with no  
431 treatment needed and treatment indicated nAMD as well as between stabilised and retreatment  
432 indicated situations based on SD-OCT raw data. These algorithms can be applied to daily  
433 practice to support the decision of non-retina specialists for referral to treatment centres. The  
434 defining characteristics of these algorithms are end-to-end processing and their independence  
435 of specific OCT feature analysis. In addition, the saliency map viewer could visualize the  
436 relevant characteristics for the algorithms. In previous studies the developed AI algorithms were  
437 predominantly addressing the question of AI-assisted automatic segmentations on SD-OCT  
438 images [32, 33]. In additional AI studies on nAMD the prediction for conversion from  
439 intermediate into nAMD was of major interest [9, 14, 15], but also the analysis for predictive  
440 biomarkers for AMD progression from intermediate AMD into nAMD was in the focus of  
441 interest [18, 34]. Especially the AI analysis of fluid distribution during anti-VEGF therapy of  
442 nAMD could be successfully achieved [35]. This study focuses on developing AI algorithms  
443 differentiating between no treatment and treatment (initially and retreatment) in intravitreal  
444 anti-VEGF therapy in nAMD.

445 In these and other AMD studies [15, 16, 36] an AUC of  $>.80$  was considered as a clinically  
446 good and meaningful differentiation. The results of the present study with an AUC of 0.927 for  
447 the differentiation between treatment-indicated nAMD and fellow eyes with AMD cases with  
448 no treatment needed can therefore be considered clinically relevant, especially because the  
449 control group of fellow eyes contained beside eyes with early and intermediate AMD, a  
450 considerable number of eyes with late stage nAMD and other pathologies. Also, the AUC of  
451 0.865 for the differentiation between stabilised and retreatment-indicated nAMD are in this  
452 relevant range. The clinical relevance of these results is also highlighted by the fact, that in both

453 situations in the IVAN and CATT trial there was also a disagreement between treating retina  
454 specialist and the RC of approximately 20% [20, 21]. Because the developed AI algorithms  
455 were based on unselected real-life treatment data and because they demonstrated robustness  
456 against downsampling, cross-validation and retinal specialist's opinion, these algorithms  
457 appear to be valid to be tested as a decision aid for referral in clinical practice.

458 In addition, the developed saliency map viewer could visualize the relevant characteristics of  
459 an individual deep learning analysis using colour coding the prediction of the trained 3D CNN  
460 models. In initial indication decisions with a predicted probability of  $\geq 97.5\%$  and an active  
461 stage of the nAMD, the retina/vitreous interface was the most important structure relevant for  
462 the activity decision of the algorithm, which may be a characteristic for retina thickness.  
463 Furthermore, changes in the subretinal space representing subretinal fluid, intraretinal cysts,  
464 sub-RPE fluid and in some SD-OCT scans analysis changes in the choroid were relevant.  
465 Therefore, using the saliency map analysis, the deep learning model could visualize areas in the  
466 SD-OCT volume scan, which supports the AI decision aid by visualizing the basic structural  
467 correlate for the examining ophthalmologist.

468 Our downsampling of each of the 49 B-scans of one SD-OCT volume to 1/4<sup>th</sup> of the original  
469 dimensions might have led to information loss in the related biomarkers, yielding in decreased  
470 model performance. Comparison experiments using the developed model architecture showed  
471 that the full-sized volumes decreased scores against expectation. However, the model was not  
472 fully optimized for full-size volumes and the sample size might be too small for the increased  
473 number of features. In everyday clinical practice retina specialists base their diagnostic decision  
474 also on additional information, such as fundus images, BCVA, patients age and activity criteria  
475 which could be integrated into a clinical decision aid.

476 The cohorts used in this study were data of unselected case series of the clinical routine in the  
477 Department of Ophthalmology, St. Franziskus-Hospital, Muenster. Therefore, for retreatment  
478 some individual SD-OCT images were considered as stabilised in which the treatment was

479 terminated because further anti-VEGF treatment was not considered to improve the situation.  
480 Eliminating these cases and re-evaluating all decisions from the learning cohort as well as  
481 increasing in the number of SD-OCT volume scans by developing automatization method for  
482 SD-OCT-data transfer may result in significant further qualitative improvement of individual  
483 predictions. Even though the saliency map focused clinically relevant areas, they should be  
484 interpreted with caution, since data set was small in relation to the diversity of patterns in the  
485 images.

486 In summary, the results of our study demonstrate, that the developed AI algorithms can have  
487 great implications for the future development of medical care models between non-retina and  
488 retina specialists in the treatment of patients with nAMD in real-life clinical practice. These  
489 models also offer the possibility of being extended to collaborations between non-physician  
490 providers and retina specialists. The analysis of SD-OCT scans of AMD patients with initial or  
491 repeated indications for anti-VEGF therapy in nAMD using this algorithm may support non-  
492 retina specialists in their decision for referral to a treatment centre. In addition, the individual  
493 decision of the algorithm can be supervised by saliency map volume scan visualization. This  
494 algorithm can therefore improve the performance and accuracy of non-retina specialists in real  
495 life to achieve reading centre standard.



496 **Declarations**

497 **Funding:** This study was funded by Novartis Pharma GmbH, Nuernberg, Germany.

498 The sponsor or funding organization had no role in the design or conduct of this research.

499 **Conflicts of interest:**

500 All authors certify that they have no affiliations with or involvement in any organization or  
501 entity with any financial interest (such as honoraria; educational grants; participation in  
502 speakers' bureaus; membership, employment, consultancies, stock ownership, or other equity  
503 interest; and expert testimony or patent-licensing arrangements), or non-financial interest (such  
504 as personal or professional relationships, affiliations, knowledge or beliefs) in the subject matter  
505 or materials discussed in this manuscript.

506 **Financial disclosure:** O. Ester, S. Aydin, M. Quassowski and K. Rothaus declare they have no  
507 financial interests. M. Gutfleisch received speaker honoraria from Novartis, Bayer and Zeiss  
508 outside the submitted work. G. Spital received speaker honoraria from Zeiss, OD-OS and  
509 Allergan outside the submitted work. A. Lommatzsch received speaker honoraria from  
510 Novartis, Bayer and Zeiss outside the submitted work. A. M. Dubis has a patent OCT analysis  
511 technology pending, and a patent prediction method from retinal imaging pending outside the  
512 submitted work. D. Pauleikhoff received speaker honoraria from Bayer, Novartis, Zeiss and  
513 Allergan outside the submitted work.

514 **Ethical approval:** All procedures performed in this study involving human participants were  
515 in accordance with the ethical standards of the institutional and/or national research committee  
516 and with the 1964 Helsinki Declaration and its later amendments or comparable ethical  
517 standards. Approval for the study was obtained from the local ethics committee at the  
518 University of Muenster.

519 **Informed consent:** For this type of study formal consent is not required.

## 520 References

- 521 1. Brown DM, Kaiser PK, Michels M, et al (2006) Ranibizumab versus verteporfin for  
522 neovascular age-related macular degeneration. *N Engl J Med* 355:1432–1444.  
523 <https://doi.org/10.1056/NEJMoa062655>
- 524 2. Stasch-Bouws J, Eller-Woywod SM, Schmickler S, et al (2020) [IVOM quality assurance  
525 in Westfalen-Lippe : Structure of quality assurance and results of the pilot study Q-  
526 VERA]. *Ophthalmologie* 117:336-342. <https://doi.org/10.1007/s00347-019-01030-3>
- 527 3. Brinkmann CK, Chang P, Schick T, et al (2019) [Baseline diagnostics and initial  
528 treatment decision for anti-vascular endothelial growth factor treatment in retinal  
529 diseases : Comparison between results by study physician and reading centers  
530 (ORCA/OCEAN study)]. *Ophthalmologie* 116:753–765. <https://doi.org/10.1007/s00347-018-0805-y>
- 531
- 532 4. Gulshan V, Peng L, Coram M, et al (2016) Development and Validation of a Deep  
533 Learning Algorithm for Detection of Diabetic Retinopathy in Retinal Fundus  
534 Photographs. *JAMA* 316:2402. <https://doi.org/10.1001/jama.2016.17216>
- 535 5. Lee CS, Tying AJ, Deruyter NP, et al (2017) Deep-learning based, automated  
536 segmentation of macular edema in optical coherence tomography. *Biomed Opt Express*  
537 8:3440-3448. <https://doi.org/10.1364/BOE.8.003440>
- 538 6. Burlina PM, Joshi N, Pekala M, et al (2017) Automated Grading of Age-Related Macular  
539 Degeneration From Color Fundus Images Using Deep Convolutional Neural Networks.  
540 *JAMA Ophthalmol* 135:1170–1176. <https://doi.org/10.1001/jamaophthalmol.2017.3782>
- 541 7. Abràmoff MD, Lavin PT, Birch M, et al (2018) Pivotal trial of an autonomous AI-based  
542 diagnostic system for detection of diabetic retinopathy in primary care offices. *NPJ Digit*  
543 *Med* 1:39. <https://doi.org/10.1038/s41746-018-0040-6>
- 544 8. De Fauw J, Ledsam JR, Romera-Paredes B, et al (2018) Clinically applicable deep  
545 learning for diagnosis and referral in retinal disease. *Nat Med* 24:1342–1350.  
546 <https://doi.org/10.1038/s41591-018-0107-6>
- 547 9. Russakoff DB, Lamin A, Oakley JD, et al (2019) Deep Learning for Prediction of AMD  
548 Progression: A Pilot Study. *Investig Ophthalmology Vis Sci* 60:712.  
549 <https://doi.org/10.1167/iovs.18-25325>
- 550 10. Wang Y, Tu D, Du J, et al (2019) Classification of Subcortical Vascular Cognitive  
551 Impairment Using Single MRI Sequence and Deep Learning Convolutional Neural  
552 Networks. *Front Neurosci* 13:627. <https://doi.org/10.3389/fnins.2019.00627>
- 553 11. Maetschke S, Antony B, Ishikawa H, et al (2019) A feature agnostic approach for  
554 glaucoma detection in OCT volumes. *PloS One* 14:e0219126.  
555 <https://doi.org/10.1371/journal.pone.0219126>
- 556 12. Li Z, Guo C, Nie D, et al (2020) Deep learning for detecting retinal detachment and  
557 discerning macular status using ultra-widefield fundus images. *Commun Biol* 3:15.  
558 <https://doi.org/10.1038/s42003-019-0730-x>

- 559 13. Kermany DS, Goldbaum M, Cai W, et al (2018) Identifying Medical Diagnoses and  
560 Treatable Diseases by Image-Based Deep Learning. *Cell* 172:1122-1131.e9.  
561 <https://doi.org/10.1016/j.cell.2018.02.010>
- 562 14. Liefers B, Colijn JM, González-Gonzalo C, et al (2020) A Deep Learning Model for  
563 Segmentation of Geographic Atrophy to Study Its Long-Term Natural History.  
564 *Ophthalmology* 127:1086–1096. <https://doi.org/10.1016/j.ophtha.2020.02.009>
- 565 15. Schmidt-Erfurth U, Waldstein SM, Klmscha S, et al (2018) Prediction of Individual  
566 Disease Conversion in Early AMD Using Artificial Intelligence. *Invest Ophthalmol Vis*  
567 *Sci* 59:3199–3208. <https://doi.org/10.1167/iovs.18-24106>
- 568 16. Yim J, Chopra R, Spitz T, et al (2020) Predicting conversion to wet age-related macular  
569 degeneration using deep learning. *Nat Med* 26:892-899. <https://doi.org/10.1038/s41591-020-0867-7>
- 571 17. Lee CS, Baughman DM, Lee AY (2016) Deep learning is effective for the classification  
572 of OCT images of normal versus Age-related Macular Degeneration. *Ophthalmol Retina*  
573 1:322-327. <https://doi.org/10.1016/j.oret.2016.12.009>
- 574 18. Schmidt-Erfurth U, Bogunovic H, Sadeghipour A, et al (2018) Machine Learning to  
575 Analyze the Prognostic Value of Current Imaging Biomarkers in Neovascular Age-  
576 Related Macular Degeneration. *Ophthalmol Retina* 2:24–30.  
577 <https://doi.org/10.1016/j.oret.2017.03.015>
- 578 19. Rothaus K, Farecki M-L, Mussinghoff P, et al (2019) [Analysis of the “Portal” Care  
579 Model - Examination of the Outcome Quality of IVOM Therapy with Regard to Latency  
580 Periods in Exudative AMD]. *Klin Monbl Augenheilkd* 238:293-301.  
581 <https://doi.org/10.1055/a-0982-5294>
- 582 20. IVAN Study Investigators, Chakravarthy U, Harding SP, et al (2012) Ranibizumab versus  
583 bevacizumab to treat neovascular age-related macular degeneration: one-year findings  
584 from the IVAN randomized trial. *Ophthalmology* 119:1399–1411.  
585 <https://doi.org/10.1016/j.ophtha.2012.04.015>
- 586 21. CATT Research Group, Martin DF, Maguire MG, et al (2011) Ranibizumab and  
587 bevacizumab for neovascular age-related macular degeneration. *N Engl J Med* 364:1897–  
588 1908. <https://doi.org/10.1056/NEJMoa1102673>
- 589 22. Mazzaferri J, Beaton L, Hounye G, et al (2017) Open-source algorithm for automatic  
590 choroid segmentation of OCT volume reconstructions. *Sci Rep* 7:42112.  
591 <https://doi.org/10.1038/srep42112>
- 592 23. Resampling using pixel area relation.  
593 [https://docs.opencv.org/3.4/da/d54/group\\_\\_imgproc\\_\\_transform.html](https://docs.opencv.org/3.4/da/d54/group__imgproc__transform.html). Accessed 17 Oct  
594 2021
- 595 24. Lim G, Bellemo V, Xie Y, et al (2020) Different fundus imaging modalities and technical  
596 factors in AI screening for diabetic retinopathy: a review. *Eye Vis Lond Engl* 7:21.  
597 <https://doi.org/10.1186/s40662-020-00182-7>
- 598 25. Dozat T (2016) Incorporating Nesterov Momentum into Adam.  
599 <https://openreview.net/forum?id=OM0jvwB8jIp57ZJjtNEZ>. Accessed 17 Oct 2021

- 600 26. Chollet F (2015) Keras. <https://keras.io>. Accessed 17 Oct 2021
- 601 27. Abadi M, Agarwal A, Barham P, Brevdo, E (2015) TensorFlow: Large-scale machine  
602 learning on heterogeneous systems. <https://www.tensorflow.org>. Accessed 17 Oct 2021
- 603 28. Simonyan K, Vedaldi, Andrea, Zisserman, Andrew (2014) Deep Inside Convolutional  
604 Networks: Visualising Image Classification Models and Saliency Maps. arXiv:1312.6034.  
605 <https://arxiv.org/abs/1312.6034>. Accessed 17 Oct 2021
- 606 29. Kotikalapudi R (2017) What is Saliency? [https://raghakot.github.io/keras-](https://raghakot.github.io/keras-vis/visualizations/saliency/#what-is-saliency)  
607 [vis/visualizations/saliency/#what-is-saliency](https://raghakot.github.io/keras-vis/visualizations/saliency/#what-is-saliency). Accessed 17 Oct 2021
- 608 30. Zweig MH, Campbell G (1993) Receiver-operating characteristic (ROC) plots: a  
609 fundamental evaluation tool in clinical medicine. *Clin Chem* 39:561–577.
- 610 31. Fleiss JL (1971) Measuring nominal scale agreement among many raters. *Psychol Bull*  
611 76:378–382. <https://doi.org/10.1037/h0031619>
- 612 32. Mishra Z, Ganegoda A, Selicha J, et al (2020) Automated Retinal Layer Segmentation  
613 Using Graph-based Algorithm Incorporating Deep-learning-derived Information. *Sci Rep*  
614 10:9541. <https://doi.org/10.1038/s41598-020-66355-5>
- 615 33. Maloca PM, Lee AY, de Carvalho ER, et al (2019) Validation of automated artificial  
616 intelligence segmentation of optical coherence tomography images. *PloS One*  
617 14:e0220063. <https://doi.org/10.1371/journal.pone.0220063>
- 618 34. Kurmann T, Yu S, Márquez-Neila P, et al (2019) Expert-level Automated Biomarker  
619 Identification in Optical Coherence Tomography Scans. *Sci Rep* 9:13605.  
620 <https://doi.org/10.1038/s41598-019-49740-7>
- 621 35. Schlegl T, Waldstein SM, Bogunovic H, et al (2018) Fully Automated Detection and  
622 Quantification of Macular Fluid in OCT Using Deep Learning. *Ophthalmology* 125:549–  
623 558. <https://doi.org/10.1016/j.ophtha.2017.10.031>
- 624 36. Yan Q, Weeks DE, Xin H, et al (2020) Deep-learning-based Prediction of Late Age-  
625 Related Macular Degeneration Progression. *Nat Mach Intell* 2:141-150.  
626 <https://doi.org/10.1038/s42256-020-0154-9>

627 **Figure Legends**

628 **Figure 1:** Treatment procedure for nAMD following the PRN schema with AI decision support  
629 systems for initial indication and retreatment decision

630 **Figure 2:** Final preprocessing pipeline with one sample slice from the raw image data  
631 extracted from the SD-OCT machine to the final input used to train the deep learning model

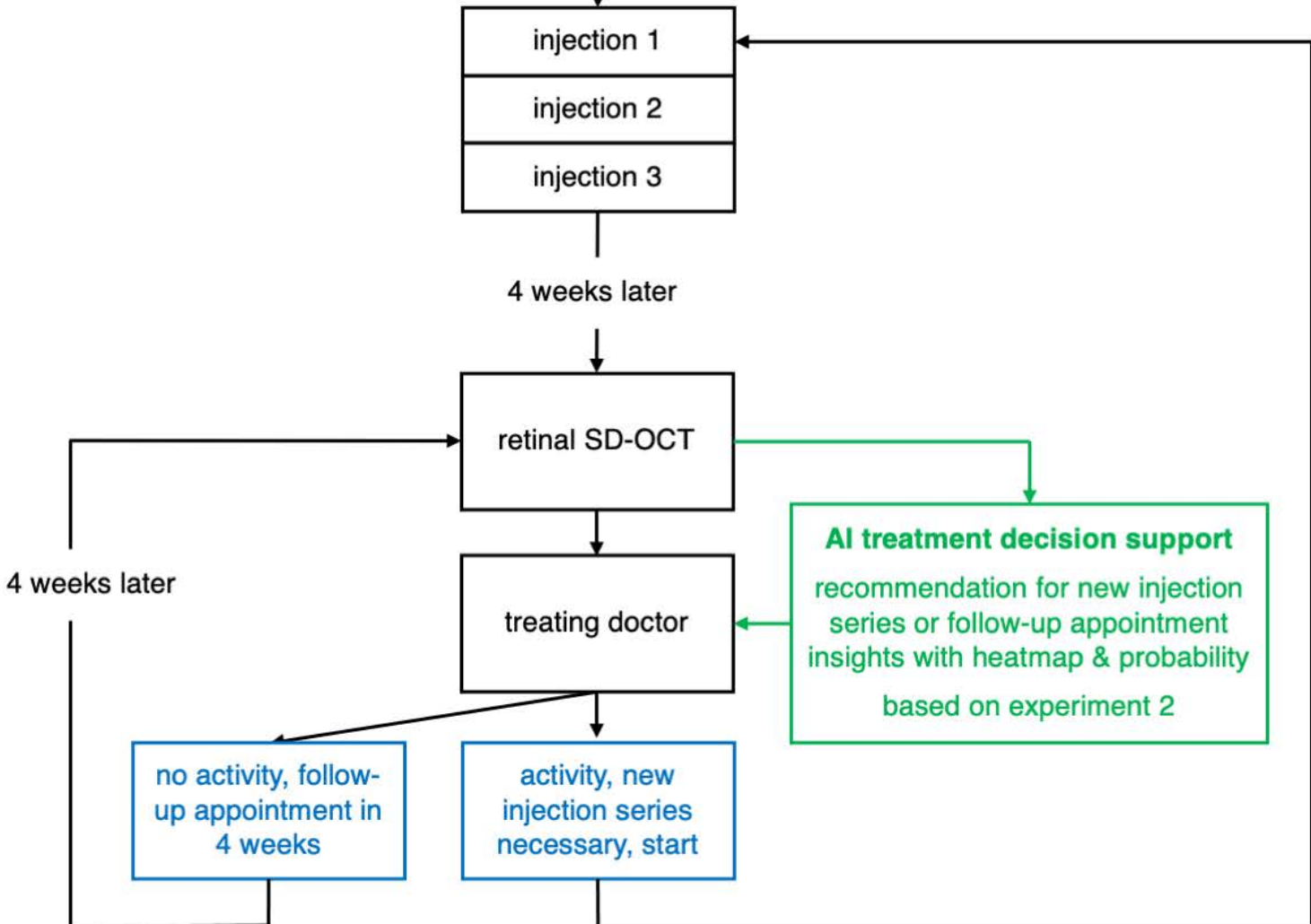
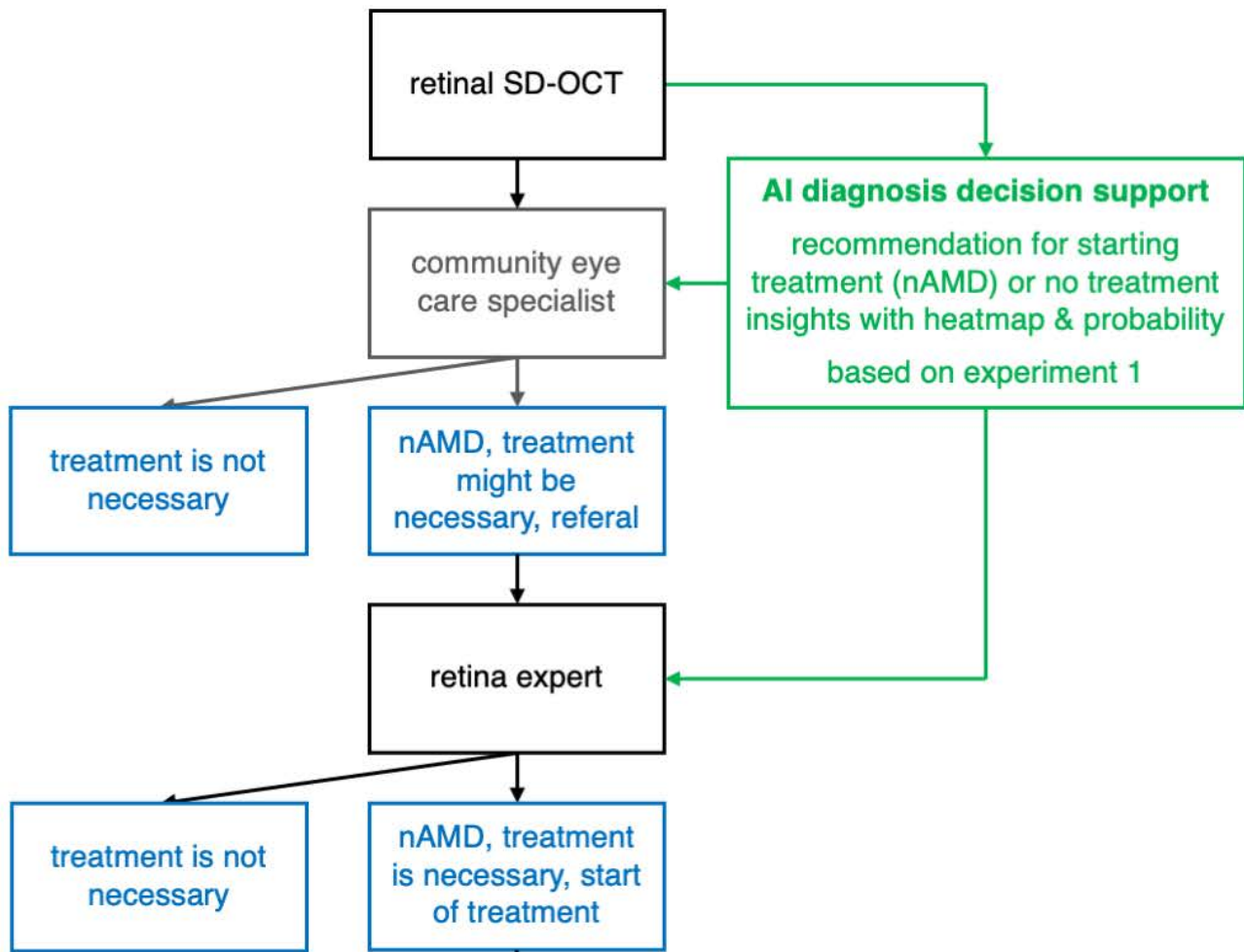
632 **Figure 3:** Illustrates the receiver operating characteristic curves (ROC) for experiment 1, the  
633 faint-coloured lines show each of the 10 folds, the thick blue line the mean of all experiments;  
634 area under receiver operating characteristic curve (AUC)

635 **Figure 4:** Frequency of the prediction value no treatment and initial treatment of AMD

636 **Figure 5:** Illustrates the receiver operating characteristic curves (ROC) for experiment 2, the  
637 faint-coloured lines show each of the 10 folds, the thick blue line the mean of all experiments;  
638 area under receiver operating characteristic curve (AUC)

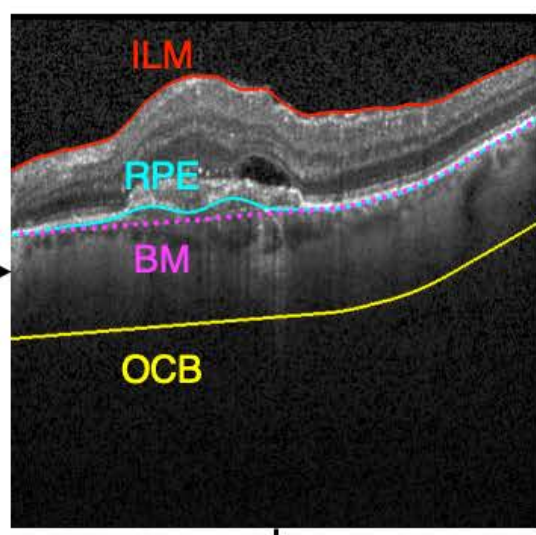
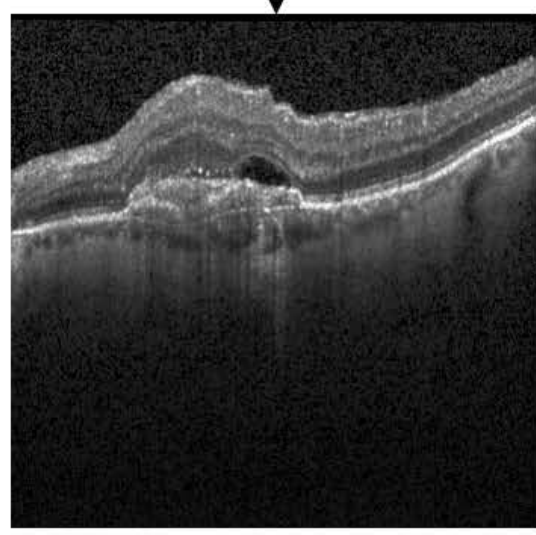
639 **Figure 6:** Frequency of the prediction value stabilised nAMD and active nAMD

640 **Figure 7:** Saliency map of one sample OCT for a single B-scan (a) and in z-axis direction  
641 across 49 B-scans (b)



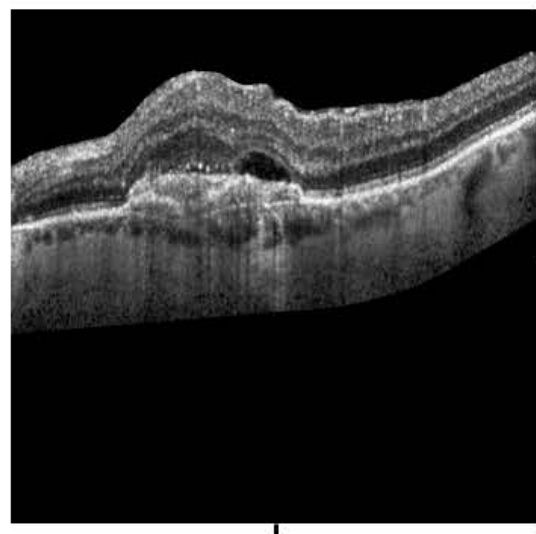
SD-OCT machine

**raw OCT image**  
single B-scan of 512x496 px  
greyscale integer values 0–255

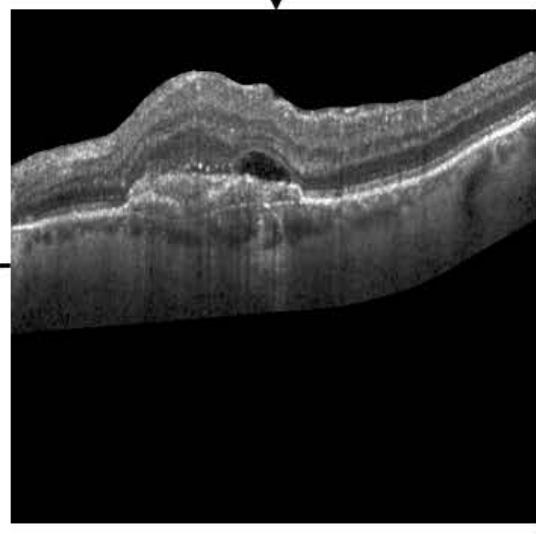


**segmentation lines**  
generated by SD-OCT  
ILM: inner limiting membrane  
RPE: retinal pigment epithelium  
calculated  
BM: Bruch's membrane  
OCB: outer chorodial boundary

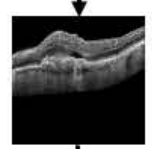
**CLAHE filter**  
increased local contrast



**ROI enhancement**  
areas outside Russakoff ROI  
(ILM to OCB) replaced  
with random noise



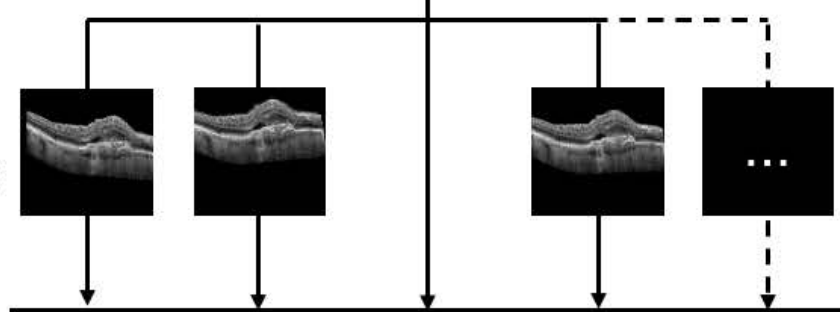
**downsampling**  
resized to 128x124 px  
using INTER\_AREA method



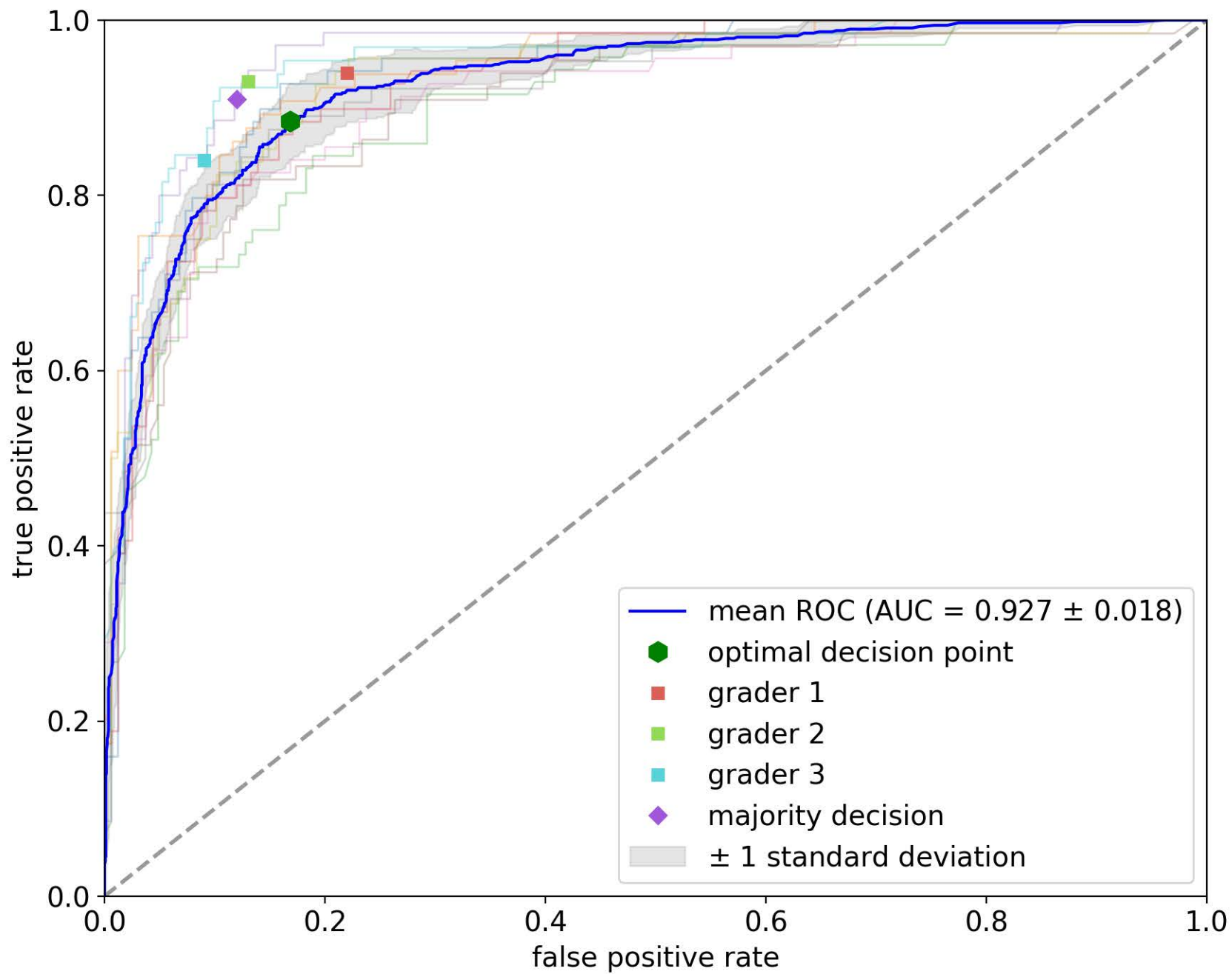
**normalize eyeside**  
horizontal flip of left eyes so all  
images have the same orientation



**data augmentation**  
random rotation, shifts  
30 variants

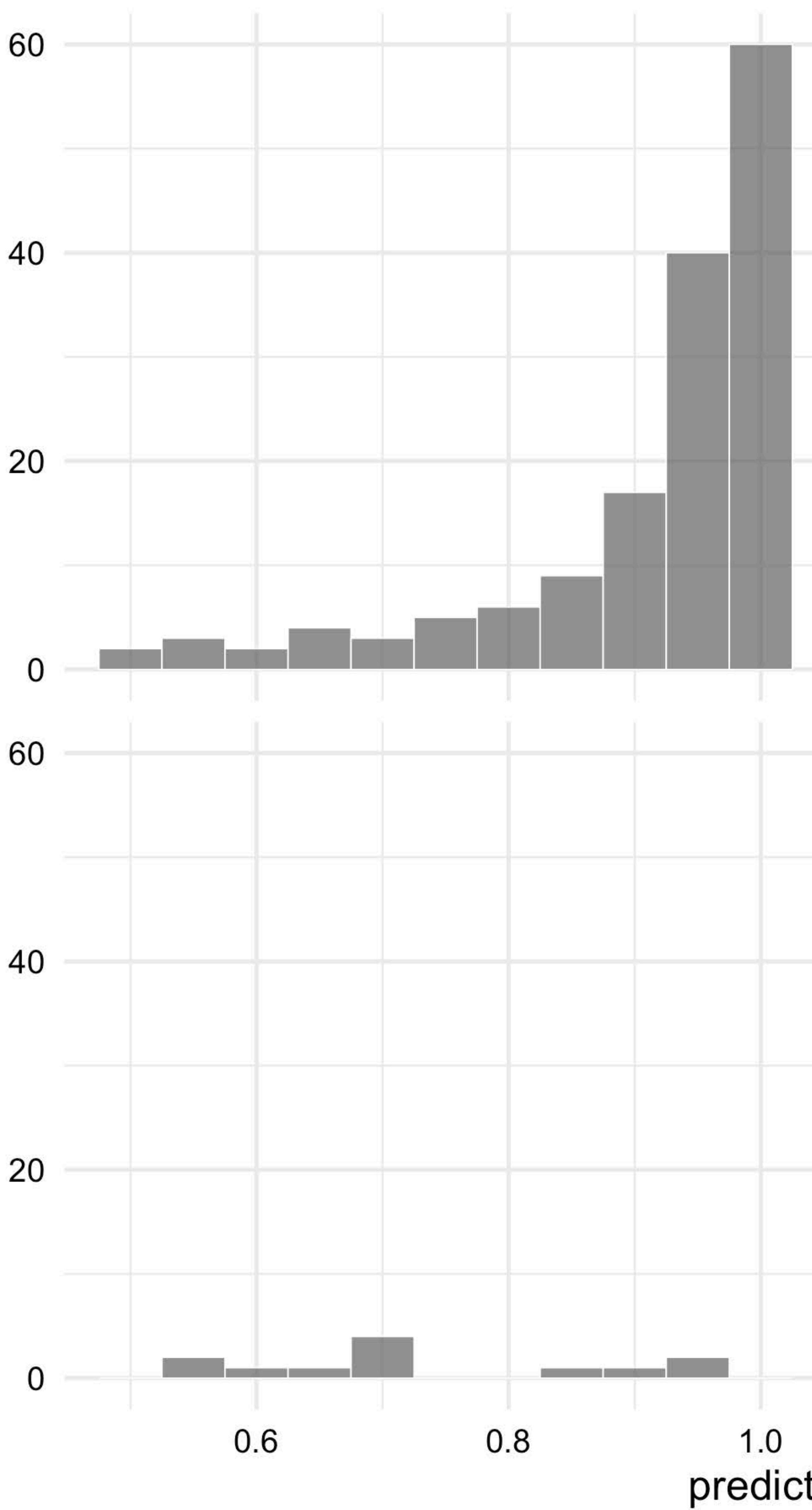


deep learning model

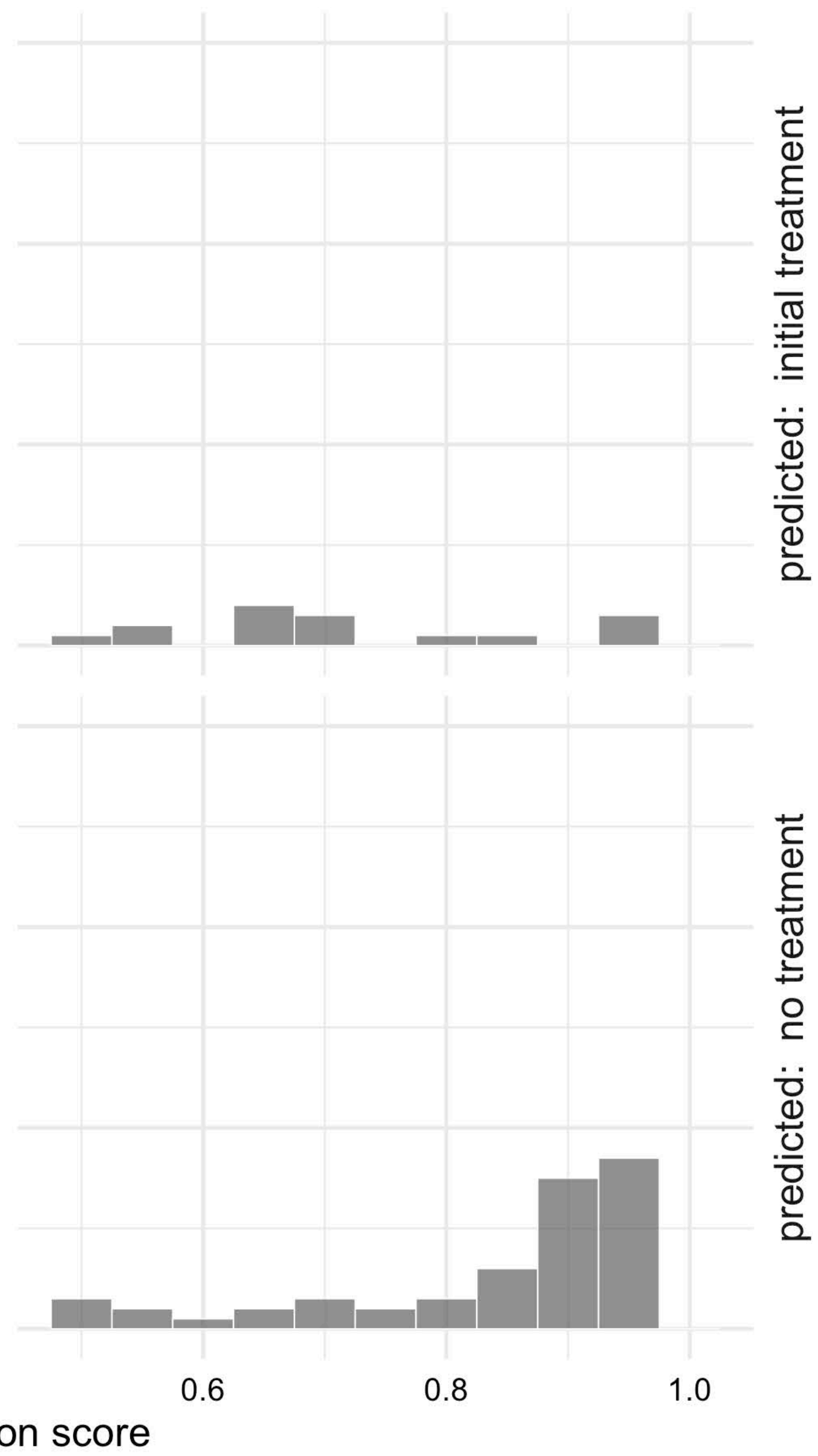


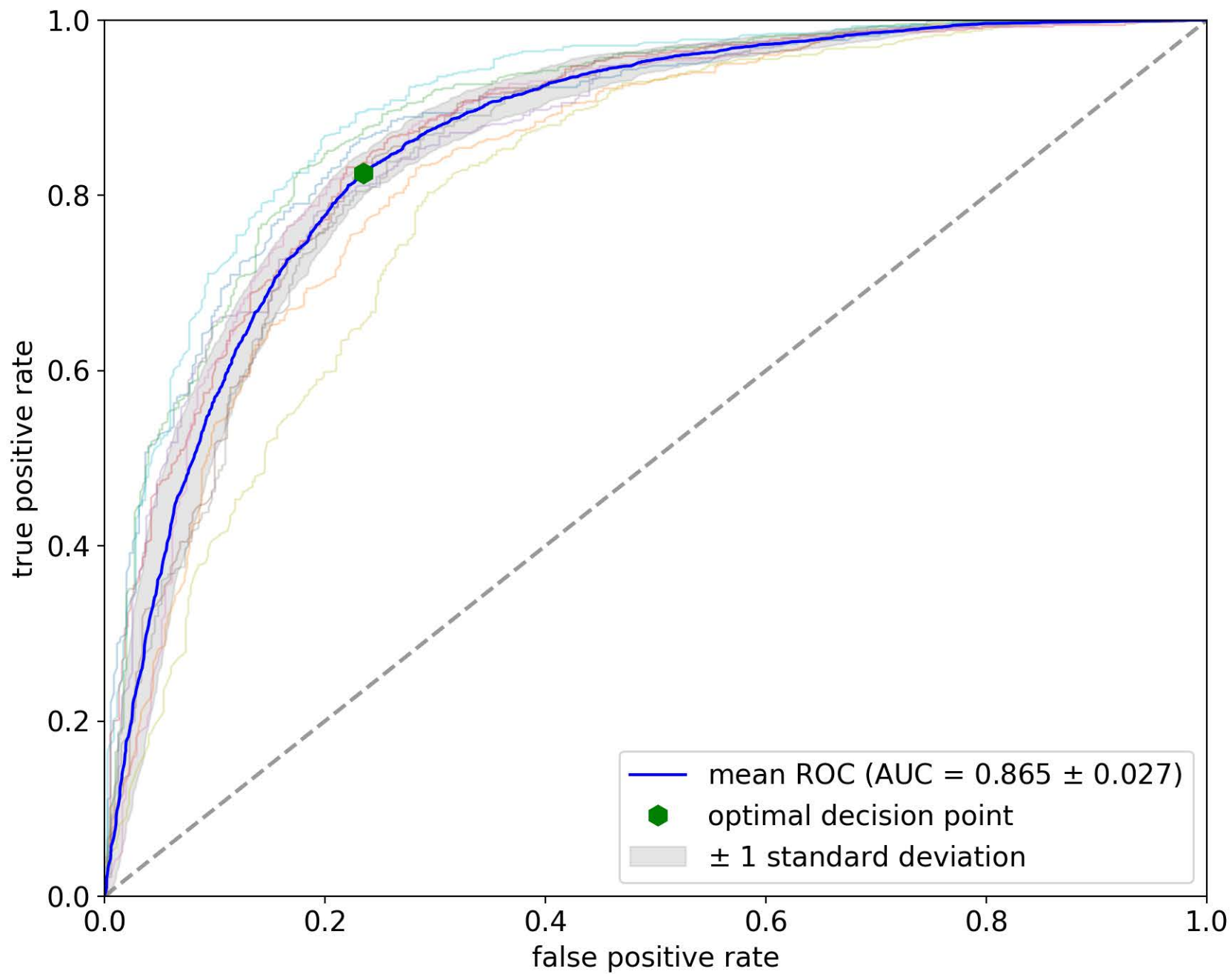


actual: initial treatment

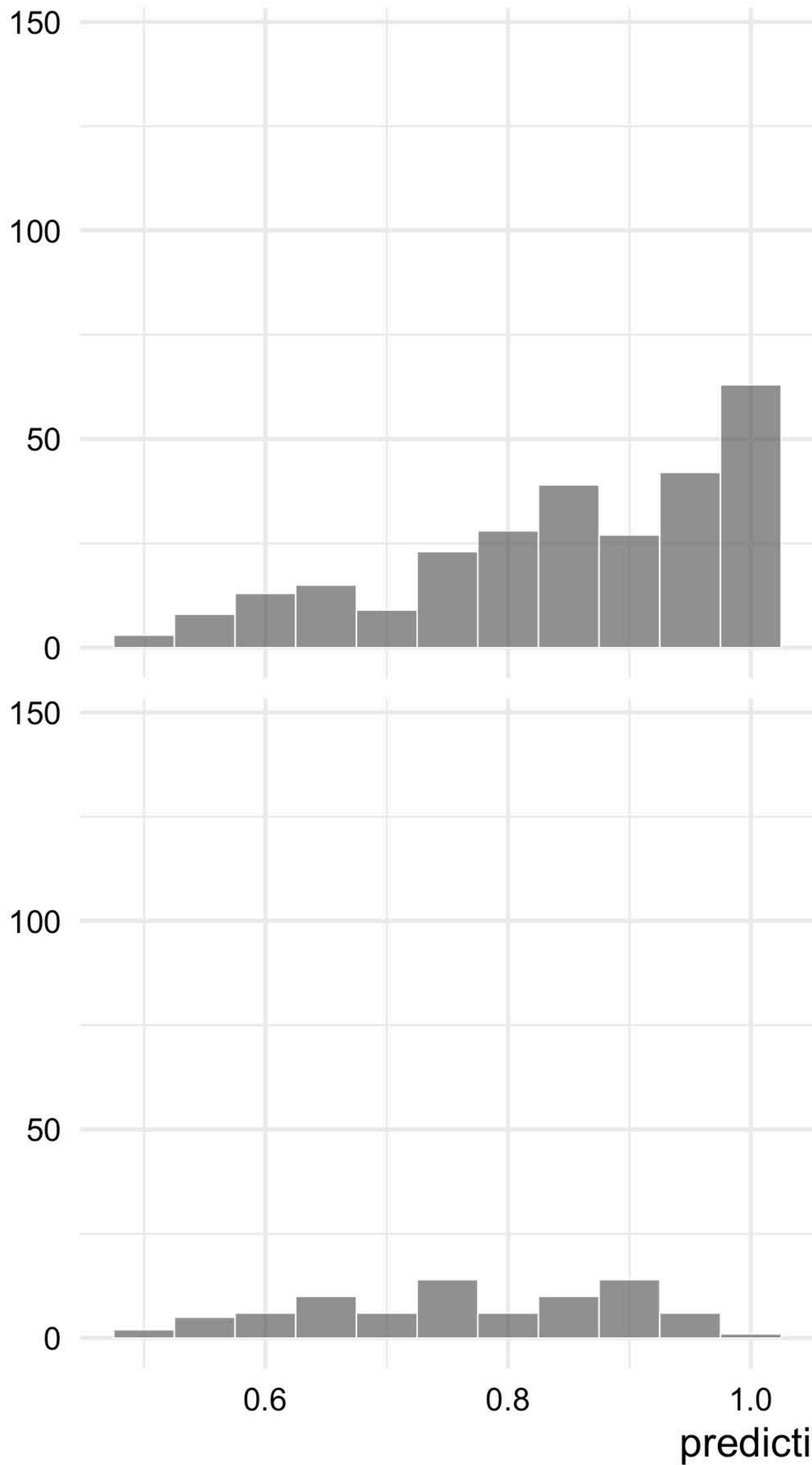


actual: no treatment

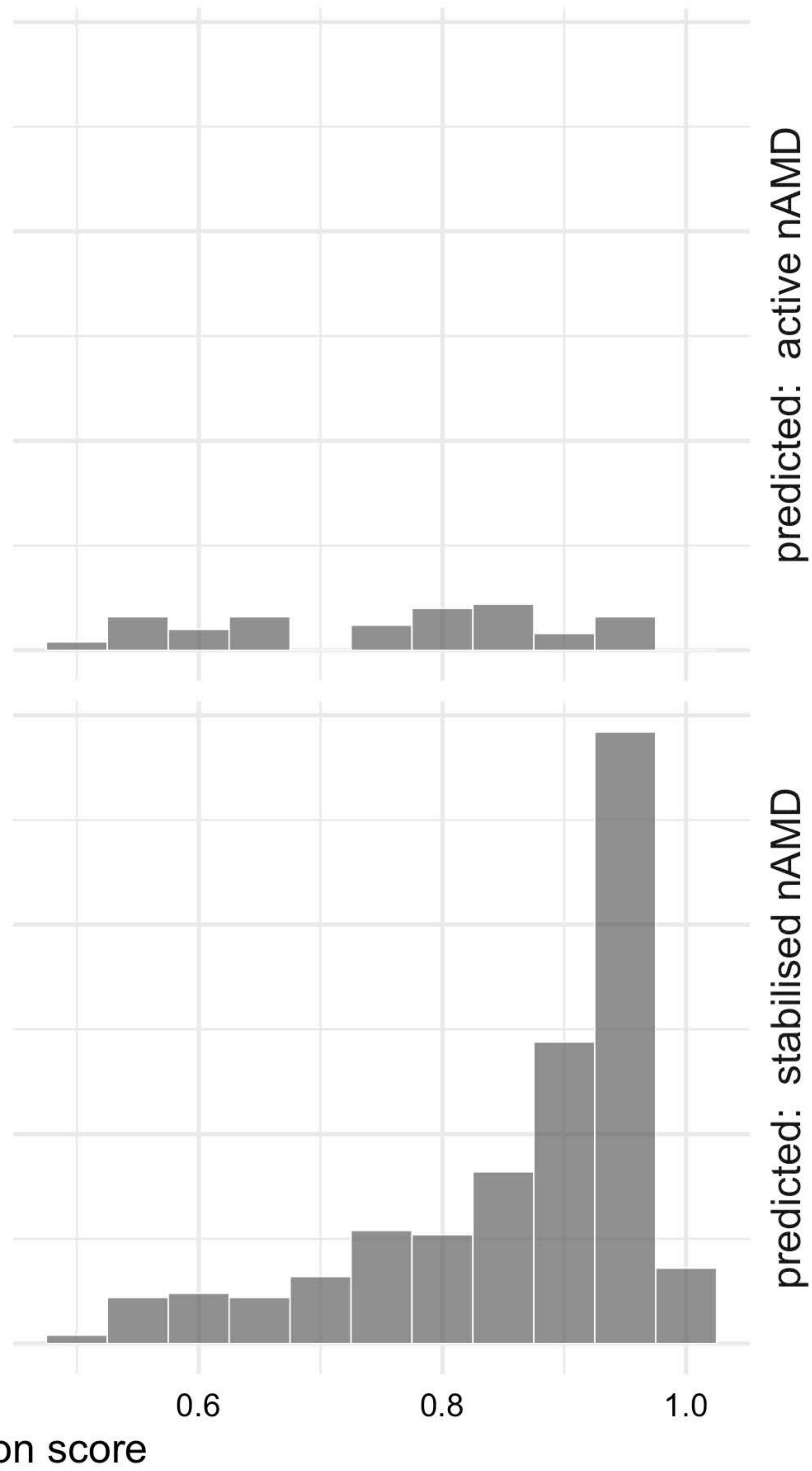




actual: active nAMD

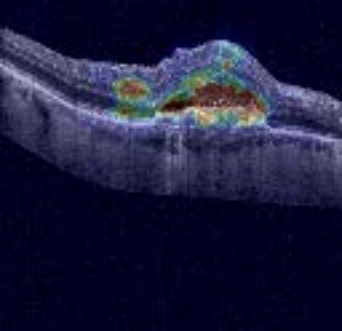


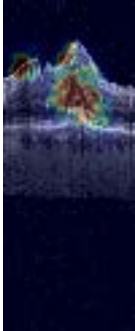
actual: stabilised nAMD



predicted: active nAMD

predicted: stabilised nAMD





## Tables

Table 1: Breakdown of “no treatment” class into subclasses for experiment 1 by expert opinion

TNR = true negative rate

definition of subclass	number of predictions		class prevalence (sum)	subclass TNR (specificity)
	Initial treatment	no treatment		
early AMD	3	137	140	98%
intermediate AMD	32	211	243	87%
geographic atrophy	12	52	64	81%
disciform scar	18	34	52	65%
other pathologies (e.g. epiretinal membrane, pattern dystrophy)	8	26	34	76%
nAMD with BCVA > 1.3 logMAR	62	76	138	55%
not graded (missing or low-quality data)	3	3	6	50%
<b>totals</b>	<b>138</b>	<b>539</b>	<b>677</b>	<b>80%</b>

Table 2: AUC results for experiment 1 and different preprocessing steps

Preprocessing	CV AUC
downsampled	0.880
downsampled, ROI	0.906
downsampled, ROI, CLAHE	0.925
<b>downsampled, ROI, CLAHE, augmentation (final)</b>	<b>0.927</b>
fullsize, ROI, CLAHE	0.894

Table 3: Parameters of the 3D-CNN architecture in experiment 1

(L2) = L2-regularization

(ReLU) = rectified linear unit

Layer	Units	Kernel Size	Activation	L2
3D convolution_1	32	3 x 3 x 3	ReLU	0.005
Batch normalization_1				
3D Max pooling_1		2 x 2 x 2		
3D convolution_2	32	3 x 3 x 3	ReLU	0.005
Batch normalization_2				
3D Max pooling_2		2 x 2 x 2		
3D convolution_3	32	3 x 3 x 3	ReLU	0.005
Batch normalization_3				
3D Max pooling_3		4 x 4 x 4		
Global Average Pooling				
Fully Connected	64			
Dropout (30%)				
Fully Connected	2		Softmax	

Table 4: Metrics of clinical experts in grading

Expert decision based only on SD-OCT

Needing initial treatment?	Grader 1		Grader 2		Grader 3		Majority	
	Yes	No	Yes	No	Yes	No	Yes	No
Yes	66	4	65	5	59	11	64	6
No	7	25	4	28	3	29	4	28
Cohen's Kappa	0.743		0.797		0.702		0.776	